Boundary Layer Dynamics in a Simple Model for Convectively Coupled Gravity Waves

MICHAEL L. WAITE* AND BOUALEM KHOUIDER

Department of Mathematics and Statistics, University of Victoria, Victoria, British Columbia, Canada

(Manuscript received 1 July 2008, in final form 19 January 2009)

ABSTRACT

A simplified model of intermediate complexity for convectively coupled gravity waves that incorporates the bulk dynamics of the atmospheric boundary layer is developed and analyzed. The model comprises equations for velocity, potential temperature, and moist entropy in the boundary layer as well as equations for the free tropospheric barotropic (vertically uniform) velocity and first two baroclinic modes of vertical structure. It is based on the multicloud model of Khouider and Majda coupled to the bulk boundary layer–shallow cumulus model of Stevens. The original multicloud model has a purely thermodynamic boundary layer and no barotropic velocity mode. Here, boundary layer horizontal velocity divergence is matched with barotropic convergence in the free troposphere and yields environmental downdrafts. Both environmental and convective downdrafts act to transport dry midtropospheric air into the boundary layer. Basic states in radiative–convective equilibrium are found and are shown to be consistent with observations of boundary layer and free troposphere climatology. The linear stability of these basic states, in the case without rotation, is then analyzed for a variety of tropospheric regimes. The inclusion of boundary layer dynamics—specifically, environmental downdrafts and entrainment of free tropospheric air—enhances the instability of both the synoptic-scale moist gravity waves and nonpropagating congestus modes in the multicloud model. The congestus mode has a preferred synoptic-scale wavelength, which is absent when a purely thermodynamic boundary layer is employed. The weak destabilization of a fast mesoscale wave, with a phase speed of 26 m s^{-1} and coupling to deep convection, is also discussed.

1. Introduction

The stably stratified tropical atmosphere is connected to the sea surface by a well-mixed layer known as the atmospheric boundary layer (ABL; e.g., Kraus and Hanson 1974; Albrecht et al. 1979; Firestone and Albrecht 1986; Betts and Ridgway 1989; Larsen et al. 1999; Johnson et al. 2001). The tropical ABL is often topped by shallow cumulus and/or stratus clouds that are sandwiched between the mixed layer and the trade wind inversion (Larsen et al. 1999; Johnson et al. 2001), a stable layer inhibiting the spontaneous occurrence of deep convection (Emanuel 1994; Mapes 2000; Majda and Khouider 2002; Khouider et al. 2003). Convective, radiative, and turbulent processes combined with downdrafts from above are believed to be key for maintaining the ABL average height at a more or less constant level over large regions of the western Pacific warm pool (Larsen et al. 1999; Johnson et al. 2001). The fluid mechanics and thermodynamics of the ABL are thus important vehicles through which latent heat from the ocean surface is transported into the free troposphere, providing the major source of energy for tropical circulation. ABL dynamics are small-scale processes that are not explicitly represented in general circulation model grid boxes; rather, they are parameterized in conjunction with cumulus convection to provide the latent heating that is necessary to drive large-scale tropical circulation and waves.

Because of the well-mixed nature of the tropical ABL, bulk boundary layer models, averaged over the mixed layer depth, are often derived and used for both theoretical and practical purposes (e.g., Arakawa and Shubert 1974; Betts 1976; Bellon and Stevens 2005; Stevens 2006, hereafter S06). Moreover, many intermediate parameterization models for tropical convection employ a purely thermodynamic boundary layer reduced to a single equation for the boundary layer moist entropy, driven solely by surface evaporation and

* Current affiliation: Department of Applied Mathematics, University of Waterloo, Waterloo, Ontario, Canada.

Corresponding author address: Dr. Michael L. Waite, Department of Applied Mathematics, University of Waterloo, Waterloo, ON N2L 3G1, Canada.
E-mail: mwaite@uwaterloo.ca

DOI: 10.1175/2009JAS2871.1

downdrafts (Emanuel et al. 1994; Yano et al. 1995, 1998; Majda and Shefter 2001a,b; Khouider and Majda 2006a, 2007, 2008a,b, hereafter KM06a, KM07, KM08a, and KM08b). Despite their crude approximation, thermodynamic bulk boundary layer models have been proven to be sufficient for sustaining inherent convective instability and maintaining convectively coupled waves in such intermediate models (Majda and Shefter 2001a,b; KM06a; KM08a). One issue of fundamental interest is how and to what extent dynamical processes in the ABL interact with convectively coupled waves and contribute to their instability. Here we couple the bulk ABL dynamical model of S06 (see also Bellon and Stevens 2005; Neggers et al. 2006) with the multicloud model of Khouider and Majda (K&M), thereby extending the boundary layer of the multicloud model to include equations for conservation of mass, momentum, and potential temperature in addition to moist entropy.

The free tropospheric dynamics of the multicloud models of K&M are based on a crude vertical truncation of the Boussinesq equations to the first two baroclinic modes of vertical structure (Mapes 2000; Majda and Shefter 2001b). The heating field assumes three profiles corresponding to three cloud types that are observed to characterize organized tropical convection (Lin and Johnson 1996; Johnson et al. 1999; Kiladis et al. 2005): low level/congestus, deep convective, and stratiform clouds. Low-level/congestus cloud decks, which are ubiquitous in dry tropospheric regions, often lead deep convection. They heat the lower troposphere, cool the upper troposphere, and serve to precondition and moisten the environment to develop and sustain deep penetrative hot towers, which are the major heat engines for convectively coupled waves. Stratiform anvils evolving in the wake of deep convection heat the upper troposphere and cool the lower troposphere through evaporation of stratiform rain. This evaporative cooling induces downdrafts, which in turn cool and dry the boundary layer. This type of downdraft is referred to here as the convective downdraft.

Linear stability analysis and numerical simulations (KM06a, KM07, KM08a, and KM08b) show that the multicloud model possesses a basic moist gravity wave instability at synoptic scales characterized by a recharge–discharge mechanism of moisture and convective available potential energy (CAPE), involving low-level moistening due to congestus clouds and drying from precipitation. The boundary layer directly affects the instability through CAPE (re-)generation and downdrafts. The resulting moist gravity waves have many interesting dynamical and morphological features in general agreement with observations of convectively coupled equatorial waves (e.g., Wheeler and Kiladis 1999), including a reduced phase speed relative to dry gravity waves and a front-to-rear vertical tilt. Linear stability results for the multicloud model with rotation (KM08b) reveal synoptic-scale instability bands located on the dispersion curves of the Kelvin, $n = 0$ eastward inertia–gravity, and $n = 1$ westward inertia–gravity waves, reminiscent of the spectral peaks of outgoing longwave radiation (OLR) shown in Wheeler and Kiladis (1999). The dynamical and morphological structures of these waves are consistent with observations. For dry tropospheric basic states, the moist gravity wave instability is replaced by an unstable, nonpropagating congestus mode (KM06a, KM08a).

The boundary layer dynamics included here induce a barotropic velocity mode in the free troposphere with nonzero horizontal velocity divergence, similar to that employed by Biello and Majda (2004) for a dry model and Sobel and Neelin (2006) for the quasi-equilibrium tropical circulation model (QTCM). This barotropic mode in turn induces large-scale vertical motion, termed here environmental downdrafts, which decreases linearly with height and directly feeds back into the dynamics of the boundary layer. Interestingly, the environmental downdrafts significantly enhance the convective instability without qualitatively affecting the overall structure of the convectively coupled waves.

The remainder of the paper is organized as follows: In section 2, the bulk boundary layer and multicloud equations are summarized following S06 and KM08a, respectively. These equations are systematically coupled with each other by assuming continuity of pressure and vertical velocity at the top of the ABL. Basic state radiative–convective equilibrium (RCE) solutions for the coupled system are then derived and compared to observations, permitting a systematic calibration of crucial boundary layer parameters. Linear stability analysis, for the case without rotation, is performed in section 3. The basic instabilities are identified and compared to the results (without a dynamically active boundary layer) of KM08a. The role of the environmental downdrafts in enhancing the instability of the moist gravity wave and congestus mode and slightly destabilizing a second baroclinic gravity wave at small scales is emphasized, and a thorough analysis of sensitivity to the most important parameters is given at the end of the section. Concluding remarks are giving in section 4, and the derivation of the boundary layer equations is sketched in the appendix, following S06.

2. Model

a. Boundary layer equations

We employ a subcloud mixed layer model based on the bulk approach of S06, with a constant depth h_b. The ABL spans $-h_b \leq z < 0$ and underlies the free troposphere

TABLE 1. Boundary layer parameters and their standard values; (N) denotes new parameters that were not present in the work of K&M.

Parameter	Value	Description
h_b	500 m	Boundary layer depth
α_m	0.2	Ratio of convective downdraft velocity to upward mass flux velocity at top of ABL (N)
κ	2	Ratio of q_t to q (N)
γ	0.5	Ratio of $\Delta_m\overline{\theta}$ to $-\Delta_m\overline{\theta}_e$ (N)
Q_{Rb}	Determined at RCE	Boundary layer radiative cooling rate (N)
τ_T	8 h	Momentum entrainment time scale (N)
C_d	0.001	Surface drag coefficient
U	2 m s^{-1}	Strength of turbulent fluctuations
τ_e	Determined at RCE	Surface evaporation time scale

with $0 \le z \le H_T$. Following S06, the boundary layer is represented as a Reynolds-averaged, well-mixed Boussinesq fluid with horizontal velocity $\mathbf{u} = (u, v)$, fluctuation potential temperature θ, and equivalent potential temperature θ_e. Vertical averaging yields prognostic ABL equations for θ_{eb}, θ_b, and $\mathbf{u}_b$, where the subscript b denotes the vertical average over $-h_b \le z \le 0$:

$$\frac{\partial\theta_{eb}}{\partial t} + \mathbf{u}_b\cdot\nabla\theta_{eb} = -\frac{E}{h_b}\Delta_t\theta_e - \frac{M_d}{h_b}\Delta_m\theta_e + \frac{1}{\tau_e}\Delta_s\theta_e - Q_{\mathrm{Rb}}, \tag{1a}$$

$$\frac{\partial\theta_b}{\partial t} + \mathbf{u}_b\cdot\nabla\theta_b = -\frac{E}{h_b}\Delta_t\theta - \frac{M_d}{h_b}\Delta_m\theta + \frac{1}{\tau_e}\Delta_s\theta - Q_{\mathrm{Rb}}, \tag{1b}$$

$$\frac{\partial\mathbf{u}_b}{\partial t} + \mathbf{u}_b\cdot\nabla\mathbf{u}_b + f\mathbf{u}_b^{\perp} = -\nabla p_b - \frac{E_u}{h_b}\Delta_t\mathbf{u} - \frac{C_dU}{h_b}\mathbf{u}_b. \tag{1c}$$

Here, f is the Coriolis parameter; $\perp$ denotes perpendicular direction, that is, $\mathbf{u}_b^{\perp} = (-v_b, u_b)$; p_b is the bulk ABL pressure (see section 2c); and Q_{Rb} is the radiative cooling rate, which is assumed constant for simplicity and diagnosed at RCE (see section 2e). The remaining terms in (1) are defined in the following paragraphs. Baroclinic advection and phase changes within the boundary layer are neglected, and all variables are nondimensionalized following the work of K&M, where $c \approx 50$ m s^{-1} is the velocity scale, $L_e \approx 1500$ km is the length scale, $T \approx 8.33$ h is the time scale, and $\overline{\alpha} \approx 15$ K is the temperature scale. Dimensional variables will occasionally be employed with the same notation when there is no risk of confusion. Boundary layer parameters introduced in this section are summarized in Table 1.

With the exception of the radiative cooling and pressure gradient terms, the right-hand side of (1) is due to vertical turbulent fluxes at the top and bottom of the ABL; horizontal fluxes are neglected. Following S06, these fluxes are written as linear combinations of bulk vertical gradients (see the appendix for a review). Three downward gradients are employed:

$$\Delta_s\phi \equiv \phi_s - \phi_b, \quad \Delta_t\phi \equiv \phi_b - \phi_t, \quad \Delta_m\phi \equiv \phi_b - \phi_m, \tag{2}$$

where $\phi = \theta_e$, θ, or $\mathbf{u}$. Subscripts s, t, and m indicate values at the surface, just above the top of the ABL, and in the midtroposphere, respectively. Surface values are assumed to be fixed, whereas low- and midtropospheric values are obtained in the following section.

The strength of the surface scalar flux is given by the evaporation time scale τ_e; the surface momentum flux is characterized by the drag coefficient C_d and turbulent velocity U. We take τ_e, C_d, and U to be external parameters, with τ_e diagnosed at RCE (see section 2e). The assumption of constant τ_e follows the approach of K&M and avoids the use of wind-induced surface heat exchange (WISHE), which is not observed to play an important role in the dynamics of convectively coupled Kelvin waves (Straub and Kiladis 2003; KM06a). Because we are not explicitly modeling oceanic processes, the constant evaporation rate can be viewed as the direct response of the sea surface to solar forcing.

At the top of the ABL, the scalar flux velocity is assumed to have upward and downward contributions M_u and M_d, with the latter resulting from deep convective downdrafts [e.g., Raymond 1995; S06; see Eq. (A4) in the appendix]. We close M_u and M_d in terms of ABL and free tropospheric variables in section 2d. The momentum flux at the top of the ABL is described by a specified time scale τ_T of turbulent mixing across $z = 0$; the momentum effects of downdrafts are not included. The different treatment of thermodynamic and momentum fluxes is consistent with the neglect of cumulus friction and convective momentum transport in the free troposphere and also with the neglect of momentum effects of downdrafts by K&M. These assumptions allow us to employ the original multicloud equations in the free troposphere, modified only to include the barotropic wind (see section

2b). The turbulent fluxes combine in (1) to yield the entrainment of free tropospheric scalars and momentum into the boundary layer. The scalar and momentum entrainment velocities (following the ideas of S06) are

$$E \equiv (M_u - M_d + h_b \nabla \cdot \mathbf{u}_b)^+, \quad E_u \equiv \left(\frac{h_b}{\tau_T} + h_b \nabla \cdot \mathbf{u}_b\right)^+, \tag{3}$$

where the switch $(\cdot)^+$ denotes the nonnegative part and ensures that negative entrainment rates (an artifact of our assumption of constant ABL depth) do not occur in regions of strong ABL convergence. Apart from this switch, (3) follows without approximation from the turbulent fluxes in (A4).

Equation (1a) is a more general version of the boundary layer equivalent potential temperature equation employed by K&M. Along with downdrafts and surface fluxes, which were considered by K&M, (1a) includes advection, entrainment, and radiative cooling. Its solution requires $\mathbf{u}_b$, which depends in turn on θ_b through the boundary layer pressure. The K&M model must be modified to account for coupling with the dynamically active boundary layer; these equations are considered next.

b. Free troposphere equations

Following the work of K&M, the free tropospheric equations are derived by Galerkin projection of the Reynolds-averaged, uniformly stratified, hydrostatic Boussinesq equations onto the barotropic and first two baroclinic modes of vertical structure (e.g., Majda 2003). The tropospheric horizontal velocity $\mathbf{u}$ and fluctuation potential temperature θ are approximated by

$$\mathbf{u} = \mathbf{u}_0 + G(z)\,\mathbf{u}_1 + G(2z)\,\mathbf{u}_2, \tag{4a}$$

$$\theta = G'(z)\,\theta_1 + 2G'(2z)\,\theta_2, \tag{4b}$$

where $G(z) = \sqrt{2}\cos(\pi z/H_T)$, $G'(z) = \sqrt{2}\sin(\pi z/H_T)$, and $\mathbf{u}_j$ and θ_j are independent of z. Continuity of vertical velocity at the top of the ABL implies that it will be generally nonzero at the base of the free troposphere. We satisfy this boundary condition by allowing $\mathbf{u}_0$ to have nonzero horizontal divergence. In the absence of a dynamically active boundary layer, $\nabla \cdot \mathbf{u}_0$ must be zero. Here, however, we define $\nabla \cdot \mathbf{u}_0 \equiv -\delta_b \nabla \cdot \mathbf{u}_b$, where $\delta_b \equiv h_b/H_T$. With a rigid lid at the upper boundary, $\mathbf{u}_b$ and $\mathbf{u}_0$ induce a continuous piecewise linear vertical velocity (Biello and Majda 2004; Sobel and Neelin 2006), which is given by

$$w_0 \equiv \begin{cases} -\left(1 + \dfrac{z}{h_b}\right) h_b \nabla \cdot \mathbf{u}_b, & -h_b \le z < 0, \\ -\left(1 - \dfrac{z}{H_T}\right) h_b \nabla \cdot \mathbf{u}_b, & 0 \le z \le H_T. \end{cases} \tag{5}$$

The boundary layer flow therefore drives a closed circulation through the depth of the troposphere (Fig. 1), which allows for the exchange of mass between the ABL and free troposphere. Moisture is represented as in the work of K&M by q, the vertically averaged specific humidity fluctuation.

The vertical structure of the model is summarized in Fig. 2, in which the levels corresponding to subscripts s, t, and m in (2) are marked. By letting $z \to 0^+$ in (4), we obtain the velocity and potential temperature fluctuation at the top of the ABL:

$$\mathbf{u}_t \equiv \mathbf{u}_0 + \sqrt{2}(\mathbf{u}_1 + \mathbf{u}_2), \quad \theta_t \equiv 0. \tag{6}$$

Moisture at the top of the ABL is assumed to be proportional to the free tropospheric vertical average; that is, $q_t \equiv \kappa q$, where $\kappa > 1$ is a specified parameter. It then follows that equivalent potential temperature at the top of the ABL is $\theta_{et} \equiv \theta_t + q_t \equiv \kappa q$. Midtropospheric values for θ and θ_e are defined as in KM06a:

$$\theta_m \equiv \frac{2\sqrt{2}}{\pi}(\theta_1 + \alpha_2\theta_2), \quad \theta_{em} \equiv \frac{2\sqrt{2}}{\pi}(\theta_1 + \alpha_2\theta_2) + q, \tag{7}$$

where $0 \le \alpha_2 < 1$; θ_m and θ_{em} are vertical averages with small contributions from θ_2 representative of the lower midtroposphere. Parameters in the free troposphere equations are summarized in Table 2; standard values are employed following KM08a.

The resulting equations for the barotropic and baroclinic modes are

$$\frac{\partial \mathbf{u}_0}{\partial t} + \mathbf{u}_0 \cdot \nabla \mathbf{u}_0 = -f\mathbf{u}_0^\perp - \nabla p_0 - \nabla \cdot \mathbf{u}_0(\mathbf{u}_0 - \mathbf{u}_b) + \frac{E_u}{H_T}\Delta_t \mathbf{u}, \tag{8}$$

$$\frac{\partial \mathbf{u}_j}{\partial t} + \mathbf{u_0} \cdot \nabla \mathbf{u}_j + \mathbf{u}_j \cdot \nabla \mathbf{u_0} = -f\mathbf{u}_j^\perp + \nabla \theta_j - \frac{1}{\tau_R}\mathbf{u}_j + d_j, \tag{9}$$

$$\frac{\partial \theta_1}{\partial t} + \mathbf{u}_0 \cdot \nabla \theta_1 - \nabla \cdot \mathbf{u}_1 + \sqrt{2}\nabla \cdot \mathbf{u}_0 = H_d + \xi_s H_s + \xi_c H_c - Q_{R1} - \frac{1}{\tau_D}\theta_1, \tag{10a}$$

$$\frac{\partial \theta_2}{\partial t} + \mathbf{u}_0 \cdot \nabla \theta_2 - \frac{1}{4}\nabla \cdot \mathbf{u}_2 + \frac{\sqrt{2}}{4}\nabla \cdot \mathbf{u}_0 = -H_s + H_c - Q_{R2} - \frac{1}{\tau_D}\theta_2, \tag{10b}$$

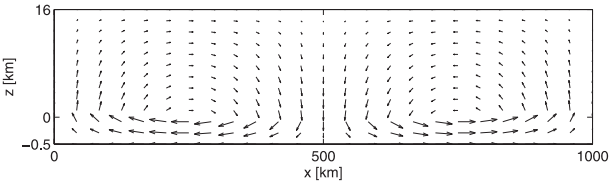

FIG. 1. A schematic of the tropospheric velocity field induced by a sinusoidal boundary layer velocity with a wavelength of 1000 km. The depth of the boundary layer is exaggerated for clarity.

where $j = 1, 2$. These equations are equivalent to the dynamical core in KM08a with three modifications: a barotropic mode (8) is included, the divergent part of which is obtained from $\mathbf{u}_b$ (see section 2c for a derivation of the barotropic pressure p_0); a new formulation of boundary layer drag d_j (given in section 2d) is employed for consistency with the momentum entrainment term in (1c); and advection of basic state potential temperature has a vertical barotropic contribution, given by the $\nabla \cdot \mathbf{u}_0$ terms on the left-hand side of (10). The interested reader is referred to KM08a for a detailed discussion of the remaining terms in these equations. Briefly, τ_R and τ_D are Rayleigh drag and Newtonian cooling time scales; Q_{Rj} is the radiative cooling rate of mode j, which is assumed to be constant and horizontally uniform; and H_d, H_c, and H_s represent deep, congestus, and stratiform convective heating rates, respectively. According to (10), H_d has the half-sine vertical structure of θ_1, whereas H_c and H_s have the full-sine structure of θ_2. Deep convection correspondingly heats the full depth of the troposphere; congestus clouds warm the lower troposphere while cooling the upper troposphere by detrainment in the midtroposphere; and stratiform clouds warm the upper troposphere while cooling the lower troposphere by the evaporation of stratiform rain. We close H_d, H_c, and H_s in terms of ABL and free tropospheric variables following KM08a, as summarized in Table 3. Notice that an important switch function is used to favor either congestus or deep convection according to whether the midtroposphere is dry or moist, respectively.

Approximations have been made to the full dynamical equations to obtain (8)–(10). First, nonlinear baroclinic–baroclinic interactions are omitted for clarity but would be straightforward to include (e.g., Stechmann et al. 2008). Second, boundary layer entrainment and detrainment of sensible heat is included in the tropospheric moisture budget to conserve moist entropy [see (11) below]. Third, barotropic vertical advection of baroclinic perturbations, which is expected to be small relative to baroclinic vertical advection, is not included. Neglecting these terms ensures conservation of vertically integrated dry static energy for adiabatic dynamics.

The equation for the vertically averaged free tropospheric moisture fluctuation q is

$$\frac{\partial q}{\partial t} + \mathbf{u}_0 \cdot \nabla q + \nabla \cdot [(\mathbf{u}_1 + \tilde{\delta}\mathbf{u}_2)\, q + (\mathbf{u}_1 + \tilde{\lambda}\mathbf{u}_2)\, \tilde{Q} - \mathbf{u}_0\, \tilde{Q}_0] = -\frac{2\sqrt{2}}{\pi}(H_d + \xi_s H_s + \xi_c H_c) + \frac{E}{H_T}\Delta_t \theta_e + \left(\frac{M_d}{H_T} + \nabla \cdot \mathbf{u}_0\right)\Delta_m \theta_e, \tag{11}$$

which is the moisture equation from KM08a with the addition of boundary layer entrainment and barotropic vertical advection (see Khouider and Majda 2006b, hereafter KM06b, for a detailed derivation in the case of a purely thermodynamic boundary layer). The new $\tilde{Q}_0$ term represents advection of the basic state moisture by w_0; it is derived in the same fashion as $\tilde{Q}$ and $\tilde{\lambda}$ in

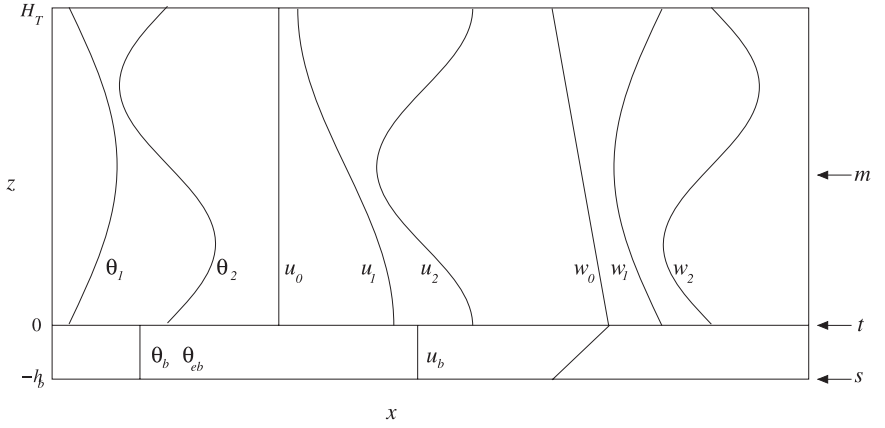

FIG. 2. A schematic of the vertical structure of the model. The levels corresponding to subscripts s, t, and m are indicated on the right.

TABLE 2. Free troposphere parameters and values employed. For parameters not determined at RCE, standard values are used (see KM08a, KM08b); (N) denotes new parameters that were not present in the work of K&M.

Parameter	Value	Description
H_T	16 km	Free troposphere depth
Q_{R1}	1 K day^{-1}	First baroclinic radiative cooling rate
Q_{R2}	Determined at RCE	Second baroclinic radiative cooling rate
τ_R	75 days	Rayleigh drag time scale
τ_D	50 days	Newtonian cooling time scale
ξ_s	0.5	Stratiform contribution to first baroclinic heating
ξ_c	1.25	Congestus contribution to first baroclinic heating
$\tilde{Q}$	0.9	Background moisture stratification
$\tilde{Q}_0$	6.5	Background contribution to barotropic vertical moisture advection (N)
$\tilde{\lambda}$	0.8	Coefficient of $\mathbf{u}_2$ in linear moisture convergence
m_0	Determined at RCE	Large-scale background downdraft velocity
μ	0.25	Contribution of convective downdrafts to M_d
α_s	0.25	Stratiform adjustment coefficient
α_c	0.1	Congestus adjustment coefficient
τ_s	3 h	Stratiform adjustment time scale
τ_{conv}	2 h	Convective time scale
τ_c	1 h	Congestus adjustment time scale
$\overline{Q}$	Determined at RCE	Bulk convective heating at RCE
a_1	0.45	Relative contribution of θ_{eb} to deep convection
a_2	0.55	Relative contribution of q to deep convection
a_0	7	Inverse convective buoyancy time scale of deep clouds
α_0'	2	Inverse convective buoyancy time scale of congestus clouds
γ_2	0.1	Relative contribution of θ_2 to deep heating
γ_2'	2	Relative contribution of θ_2 to congestus heating
α_2	0.1	Relative contribution of θ_2 to θ_{em}

KM06a, that is, by projecting the basic state moisture onto the barotropic basis function. For a basic state moisture profile $Q(z) = q_0 \exp(-z/H_q)$, it can be shown that

$$\tilde{Q}_0 = q_0 \left\{ 1 + \frac{H_q}{H_T} [\exp(-H_T/H_q) - 1] \right\}. \quad (12)$$

The standard values for $\tilde{\delta}$, $\tilde{\lambda}$, and $\tilde{Q}$ yield $\tilde{Q}_0 = 6.5$ (cf. KM06b). The last two terms on the right-hand side of (11) represent entrainment and downdrafts, respectively. They account for free tropospheric moistening and drying due to detrainment of shallow cumulus clouds, evaporation of stratiform rain, and entrainment of free troposphere air into the boundary layer. Vertically integrated moist static energy is conserved by (1a), (10), and (11) in the absence of convection and radiation for $\tau_R, \tau_D, \tau_e \to \infty$.

To close the system of model equations given by (1) and (8)–(11), we require expressions for the boundary layer and barotropic pressures p_b and p_0, the updraft and downdraft velocities M_u and M_d, and the drag d_j. These closures are described next.

TABLE 3. Convective parameterization variables and equations.

Term	Description	Equation
H_d	Deep convective heating rate	$H_d = (1 - \Lambda) Q_d$
H_s	Stratiform heating rate	$\frac{\partial H_s}{\partial t} = \frac{1}{\tau_s}(\alpha_s H_d - H_s)$
H_c	Congestus heating rate	$\frac{\partial H_c}{\partial t} = \frac{1}{\tau_c}(\alpha_c \Lambda Q_c - H_c)$
Q_d	Maximum available energy for deep convection	$Q_d = \left\{ \overline{Q} + \frac{1}{\tau_{\text{conv}}}[a_1\theta_{eb} + a_2 q - a_0(\theta_1 + \gamma_2\theta_2)] \right\}^+$
Q_c	Maximum available energy for congestus	$Q_c = \left\{ \overline{Q} + \frac{1}{\tau_{\text{conv}}}[\theta_{eb} - a_0'(\theta_1 + \gamma_2'\theta_2)] \right\}^+$
Λ	Moisture switch function	$\Lambda \equiv \begin{cases} 1, & \text{for } \Delta_m\theta_e \geq 20 \text{ K}, \\ 0, & \text{for } \Delta_m\theta_e \leq 10 \text{ K}, \\ \text{linear and continuous}, & \text{for } 10 \text{ K} \leq \Delta_m\theta_e \leq 20 \text{ K}. \end{cases}$

c. Mechanical coupling

Continuity of pressure at $z = 0$ yields mechanical coupling of the ABL to the free troposphere (Biello and Majda 2004; Sobel and Neelin 2006). We assume a hydrostatic boundary layer with a linear vertical pressure profile, which are appropriate approximations at the large horizontal scales of convectively coupled waves. By taking the divergence of (1c) and (8), and noting that the pressure at the top of the ABL is $p_0 - \sqrt{2}(\theta_1 + \theta_2)$, we obtain diagnostic equations for p_b and p_0:

$$-(1+\delta_b)\nabla^2 p_b = \nabla^2\left(\sqrt{2}(\theta_1+\theta_2)+\frac{\pi}{2}\delta_b\theta_b\right)+\frac{C_d U}{H_T}\nabla\cdot u_b + \frac{\partial^2}{\partial x_i \partial x_j}(u_{0i}u_{0j}+\delta_b u_{bi}u_{bj}), \tag{13a}$$

$$p_0 = p_b + \sqrt{2}(\theta_1+\theta_2)+\frac{\pi}{2}\delta_b\theta_b. \tag{13b}$$

The boundary layer pressure depends linearly on the free troposphere temperature perturbations, boundary layer temperature, and surface drag and nonlinearly on the barotropic and boundary layer velocities. Because $\delta_b \ll 1$, we expect the contributions in (13a) from θ_1 and θ_2 to dominate for linear waves.

d. Boundary layer closures

Downdrafts transport air from the midtroposphere into the ABL. K&M accounted for convective downdrafts, which are forced by negative buoyancy anomalies caused by evaporation of stratiform precipitation. Our inclusion of a dynamically active boundary layer introduces environmental downdrafts, which are due to explicitly resolved flow through the top of the boundary layer. Following K&M, the mass flux velocity from large-scale and convective downdrafts is

$$D_c \equiv m_0\left[1+\frac{\mu}{\overline{Q}}(H_s - H_c)\right]^+, \tag{14}$$

where m_0 is the background velocity due to large-scale subsidence, $\overline{Q}$ is the background heating, and μ measures the strength of convective downdrafts. Both m_0 and $\overline{Q}$ are obtained at RCE (KM08a). We define the total downdraft velocity M_d to be

$$M_d \equiv (D_c + h_b \nabla\cdot\mathbf{u}_b)^+, \tag{15}$$

where the environmental downdraft velocity $h_b\nabla\cdot\mathbf{u}_b$ is simply the downward velocity at the top of the ABL. The upward mass flux velocity at the top of the boundary layer M_u is assumed to be proportional to D_c (Raymond 1995), with $\alpha_m \equiv D_c/M_u$ being a prescribed small parameter.

TABLE 4. Thermodynamic profiles at RCE; (N) denotes new parameters that were not present in the work of K&M.

Parameter	Value	Description
$\Delta_s\overline{\theta}_e$	10 K	$\theta_{es} - \theta_{eb}$ at RCE
$\Delta_s\overline{\theta}$	0 K	$\theta_s - \theta_b$ at RCE (N)
$\Delta_t\overline{\theta}_e$	5 K	$\theta_{eb} - \theta_{et}$ at RCE (N)
$\Delta_t\overline{\theta}$	0 K	$\theta_b - \theta_t$ at RCE (N)
$\Delta_m\overline{\theta}_e$	Varies	$\theta_{eb} - \theta_{em}$ at RCE
$\Delta_m\overline{\theta}$	Varies	$\theta_b - \theta_m$ at RCE (set by γ) (N)

The form of the drag on the baroclinic velocity modes depends on the profile of turbulent momentum flux through the depth of the free troposphere. Assuming that it decays rapidly above the top of the boundary layer (e.g., Stull 1988), the d_j terms in (9) are given by

$$d_j \equiv \frac{\sqrt{2}}{\tau_T}\delta_b\Delta_t\mathbf{u}. \tag{16}$$

e. Basic state

We assume a steady, spatially homogeneous basic state of the atmosphere at RCE, which is denoted by $\overline{(\cdot)}$. As in the work of K&M, we set $Q_{R1} = 1$ K day^{-1}, which fixes the RCE heating rates and Q_{R2}. The six vertical gradients of θ_e and θ (summarized in Table 4) can then be used to determine the remaining variables at RCE. Following K&M, we use the relative tropospheric moistness $\Delta_m\overline{\theta}_e$ to characterize the basic thermodynamic state of the RCE: $\Delta_m\overline{\theta}_e < 10$ K corresponds to a moist RCE dominated by deep convective heating, whereas $\Delta_m\overline{\theta}_e > 20$ K is a dry RCE dominated by congestus heating. The remaining gradients, along with the parameter α_m, are chosen to yield physically consistent basic states in qualitative agreement with observations.

Combining Eqs. (10a) and (11) and the definition of E in (3), the RCE downdraft velocity $\overline{M}_d$ is given by

$$\overline{M}_d = \frac{2\sqrt{2}}{\pi}\frac{\alpha_m H_T Q_{R1}}{(1-\alpha_m)\Delta_t\overline{\theta}_e + \alpha_m\Delta_m\overline{\theta}_e}. \tag{17}$$

We set $\Delta_t\overline{\theta}_e = 5$ K, which corresponds to a drop in specific humidity of 2 g kg^{-1} across the top of the boundary layer if thermal contributions are neglected (cf. Fig. 5 in S06). The dependence of $\overline{M}_d$ on α_m and $\Delta_m\overline{\theta}_e$ is plotted in Fig. 3a. It goes to zero at $\alpha_m = 0$ and is largest for dry basic states when $\alpha_m = 1$. For $\alpha_m \lesssim 0.3$, $\overline{M}_d$ is only weakly dependent on $\Delta_m\overline{\theta}_e$. We let $\alpha_m = 0.2$, which yields a reasonable downdraft velocity of $\overline{M}_d \approx 0.5$ cm s^{-1} (cf. Fig. 15.10 in Emanuel 1994).

The surface evaporation time scale τ_e and the boundary layer radiative cooling rate Q_{Rb} are obtained at RCE and depend on the separate gradients of θ_e and θ. We simplify

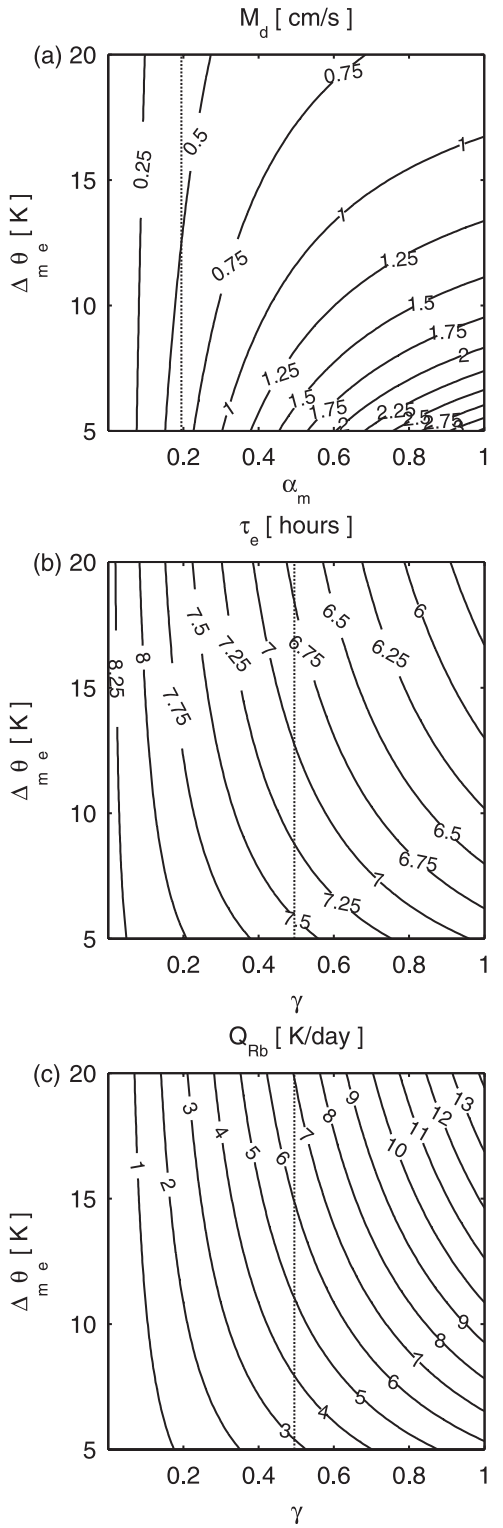

FIG. 3. (a) Downdraft velocity $\overline{M}_d$, (b) surface evaporation time scale τ_e, and (c) boundary layer radiative cooling rate Q_{Rb} at RCE; $\overline{M}_d$ is plotted as a function of α_m and $\Delta_m\overline{\theta}_e$, whereas τ_e and Q_{Rb} are plotted vs γ and $\Delta_m\overline{\theta}_e$. Standard parameter values are marked by a dotted line.

matters by neglecting the jumps in θ at the surface and ABL top; that is, we let $\Delta_s\overline{\theta} = \Delta_t\overline{\theta} = 0$. The resulting boundary layer equilibrium is a balance between warming by downdrafts and cooling by radiation. The surface jump in θ_e is fixed at $\Delta_s\overline{\theta}_e = 10$ K, as in K&M. Finally, we define the midtropospheric θ gradient from the θ_e gradient using the parameter $\gamma \equiv -\Delta_m\overline{\theta}/\Delta_m\overline{\theta}_e$. For a moist RCE with $\Delta_m\overline{\theta}_e = 11$ K, our standard value of $\gamma = 0.5$ implies an increase in θ of 5.5 K and a decrease in q of 7 g kg^{-1} from the boundary layer to the midtroposphere. The dependence of τ_e and Q_{Rb} on γ and $\Delta_m\overline{\theta}_e$ are shown in Figs. 3b,c. The evaporation time scale is maximum for small values of γ, although it remains between 5.5 and 8.5 h for a wide range of both parameters, in qualitative agreement with the results of K&M.

The boundary layer radiative cooling rate Q_{Rb} is more sensitive to the imposed parameters, particularly γ. For a given $\Delta_m\overline{\theta}_e$, larger γ implies greater drying and warming by downdrafts, which require stronger radiative cooling rates and surface moisture fluxes (i.e. larger Q_{Rb} and smaller τ_e) at RCE. Because we neglect RCE surface fluxes and entrainment of boundary layer potential temperature, Q_{Rb} is determined entirely by the warming from downdrafts. Setting $\gamma = 0$ eliminates downdraft warming and yields $Q_{Rb} = 0$, which is clearly an unrealistic limit. For a moist RCE, $\gamma = 0.5$ leads to a value of $Q_{Rb} \approx 5$ K day^{-1}, which is consistent with observations (e.g., Kraus and Hanson 1974). The fact that we obtain a reasonable value for Q_{Rb} provides a consistency check on our parameter values but does not directly affect the wave stability results described below.

3. Linear wave instability

We linearize Eqs. (1) and (8)–(11) about the RCE, neglecting Coriolis effects along with meridional variations and velocity. Perturbations from RCE are denoted by $(\cdot)' \equiv (\cdot) - \overline{(\cdot)}$. As found by K&M, the stability of convectively coupled waves depends fundamentally on the basic state tropospheric moisture $\Delta_m\overline{\theta}_e$. A synoptic-scale convectively coupled moist gravity wave instability is present for moist basic states, and a broad-band congestus standing wave instability emerges for dry states. Table 5 summarizes the wave instabilities that occur over a wide range of RCEs for the control parameters in Tables 1, 2, and 4. For comparison, corresponding instabilities with a purely thermodynamic ABL (i.e., the K&M model) are summarized in Table 6. The moist gravity wave dominates moist RCEs with $\Delta_m\overline{\theta}_e \leq 14$ K, while the congestus standing wave characterizes dry RCEs with $\Delta_m\overline{\theta}_e \geq 15$ K, in general agreement with K&M. Below we discuss the role of the boundary layer in prototypical unstable waves of each

TABLE 5. Properties of unstable waves for different basic states.

$\Delta_m\overline{\theta}_e$	Wave type	Instability wavenumber band	Wavenumber of most unstable wave	Growth rate (day^{-1}) of most unstable wave	Phase speed ($m\ s^{-1}$) of most unstable wave
11	Moist gravity	$1 \le k \le 47$	22	0.79	15.0
	Fast gravity	$k \ge 166$	Asymptotes to constant	0.36	26.2
12	Moist gravity	$2 \le k \le 46$	20	0.85	13.2
	Standing congestus	$k = 1$	1	0.14	0
	Standing stratiform	$k = 1$	1	0.034	0
	Fast gravity	$k \ge 171$	Asymptotes to constant	0.33	26.2
15	Moist gravity	$9 \le k \le 35$	14	0.74	5.5
	Standing congestus	$1 \le k \le 8$	7	0.90	0
	Standing stratiform	$1 \le k \le 8$	8	0.44	0
	Fast gravity	$k \ge 227$	Asymptotes to constant	0.21	26.2
16	Standing congestus	$1 \le k \le 29$	13	1.5	0
	Fast gravity	$k \ge 277$	Asymptotes to constant	0.17	26.2
17	Standing congestus	$1 \le k \le 123$	25	2.4	0
	Fast gravity	$k \ge 367$	Asymptotes to constant	0.12	26.2
19	Standing congestus	$k \ge 1$	39	3.8	0

type: the moist gravity wave at $\Delta_m\overline{\theta}_e = 11$ K and the congestus standing wave at $\Delta_m\overline{\theta}_e = 17$ K.

Along with the dominant moist gravity and congestus waves, the present model has two weaker instabilities that do not occur without boundary layer dynamics, as can be seen by comparing Tables 5 and 6. For intermediate RCEs with $12 \le \Delta_m\overline{\theta}_e \le 15$ K, the unstable congestus standing wave coexists with a second unstable standing wave characterized by strong stratiform heating. Its growth rate is systematically smaller than that of the congestus mode, and it disappears entirely along with the moist gravity wave for $\Delta_m\overline{\theta}_e \ge 16$.

In addition, a fast mesoscale gravity wave is weakly destabilized for all but the driest basic states with $10 < \Delta_m\overline{\theta}_e \le 18$ K, in contrast to previous results without an active boundary layer where such instability is restricted to dry basic states (e.g., KM06b). The phase speed is 26 m s^{-1}, which is approximately that of the second baroclinic dry gravity wave; indeed, the structure of the wave resembles the second baroclinic dry wave with deep convective coupling. This instability is restricted to small scales with $k \gtrsim 150$, and its growth rate, which approaches a finite limit as $k \to \infty$, is always smaller than the dominant large-scale instability. It seems to be robust to parameter changes and is intimately tied to the synoptic-scale moist gravity wave instability (see section 3d). It is unclear whether this instability is an artifact of the model boundary layer coupling or if it is physically meaningful. Its second baroclinic structure recalls the borelike waves that are known to propagate away from localized convective heat sources and to be favorable for generating new convection (e.g., Tulich et al. 2007; Stechmann et al. 2008).

a. Synoptic-scale moist gravity waves

A moist basic state with $\Delta_m\theta_e = 11$ K yields a band of unstable, convectively coupled gravity waves over $1 \le k \le 47$ (Fig. 4). The most unstable wave has phase speed $c_p \approx 15$ m s^{-1}, a growth rate of 0.8 day^{-1}, and wavenumber $k = 22$, which corresponds to a synoptic-scale wavelength of 1818 km. This phase speed and wavelength are similar to those obtained without ABL

TABLE 6. As in Table 5, but with the boundary layer dynamics turned off.

$\Delta_m\overline{\theta}_e$	Wave type	Instability wavenumber band	Wavenumber of most unstable wave	Growth rate (day^{-1}) of most unstable wave	Phase speed ($m\ s^{-1}$) of most unstable wave
11	Moist gravity	$6 \le k \le 20$	14	0.078	16.0
12	Moist gravity	$2 \le k \le 46$	13	0.17	14.3
15	Moist gravity	$4 \le k \le 16$	10	0.15	10.3
	Standing congestus	$k = 2$	2	0.018	0
16	Moist gravity	$5 \le k \le 12$	8	0.70	8.5
	Standing congestus	$k = 2$	2	0.030	0
17	Standing congestus	$k = 2$	2	0.035	0
19	Standing congestus	$k \ge 2$	Asymptotes to constant	0.21	0

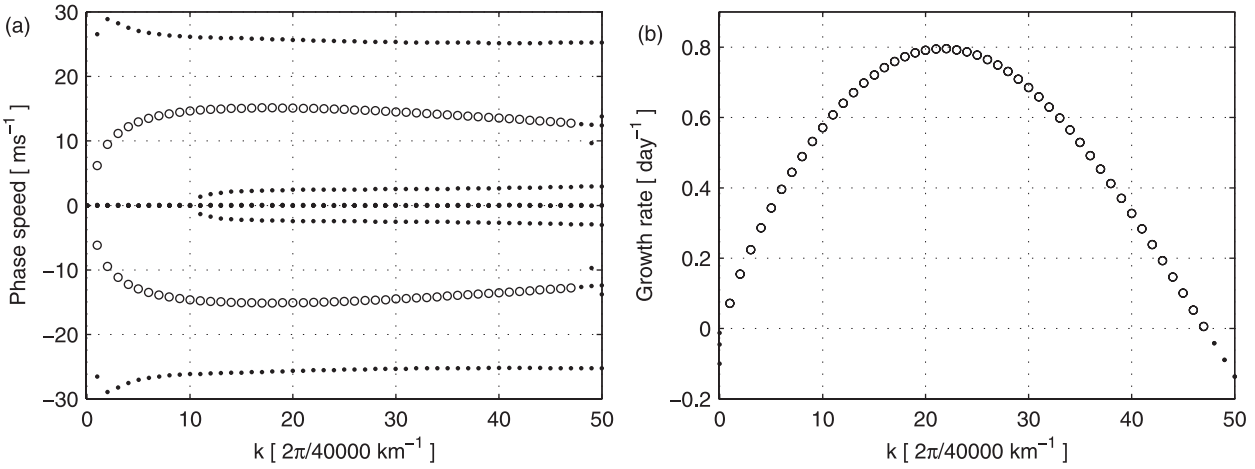

FIG. 4. (a) Phase speeds and (b) growth rates as a function of wavenumber for a moist RCE with $\Delta_m\theta_e = 11$ K. Unstable modes are drawn as open circles and stable modes as dots.

dynamics; the growth rate, however, is enhanced by an order of magnitude in the present model.

The structure of the most unstable wave at $k = 22$ is shown in Fig. 5. In the free troposphere (Figs. 5a,b), the heating, temperature, and velocity fields closely resemble the moist gravity wave obtained by K&M. The wave exhibits a strong vertical tilt, such that lower-tropospheric heating associated with congestus convection leads deep convection, which in turn leads upper-level stratiform heating. Velocity convergence in the lower troposphere occurs just before the congestus heating maximum, and vertical velocity is generally upward in the heating phase of the wave and downward in the cooling phase. For a more detailed discussion of the free tropospheric wave structure, see KM06a.

Our main interest here is in the structure of the boundary layer flow and its coupling with the free troposphere. ABL velocity is plotted in Fig. 5c. Updrafts at the top of the boundary layer occur in advance of convection and peak just before the maximum of congestus heating in the lower troposphere. Indeed, the barotropic flow through the ABL top is approximately in phase with the vertical velocity in the lower troposphere. As a result, free tropospheric air is transported into the boundary layer during the phases of stratiform heating and congestus and deep cooling; this transport drives the environmental downdrafts.

The thermodynamic structure of the boundary layer is shown in Fig. 5d. Perturbations of boundary layer potential temperature are an order of magnitude smaller than θ'_{eb}; boundary layer equivalent potential temperature can therefore be identified with ABL water vapor. This moisture leads the tropospheric vapor perturbation q', as in K&M. Boundary layer potential temperature θ'_b is out of phase with θ'_{eb} and instead leads the temperature perturbations in the lower troposphere. The phase of the ABL thermodynamic fields gives the lower troposphere a vertical tilt in agreement with the overall structure of the wave.

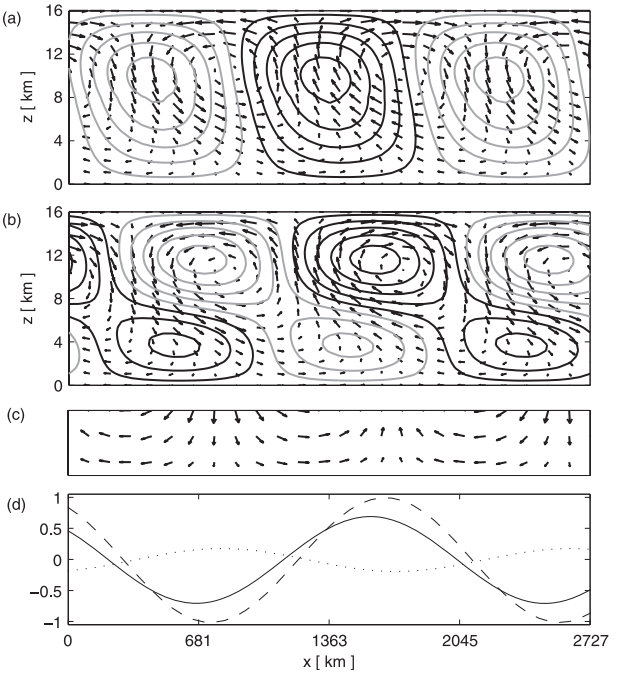

FIG. 5. Structure of the most unstable moist gravity wave for $\Delta_m\theta_e = 11$ K: perturbation of (a) convective heating; (b) potential temperature; (c) boundary layer velocity; and (d) q' (solid), θ'_{eb} (dashed), and θ'_b (dotted). In (a) and (b), positive contours are black and negative contours are gray. Note that the velocity vectors in (c) are not on the same scale as in (a) and (b). Curves in (d) are normalized by the amplitude of θ'_{eb}. The phase of the wave is chosen such that the deep convective heating maximum occurs in the center of the plot.

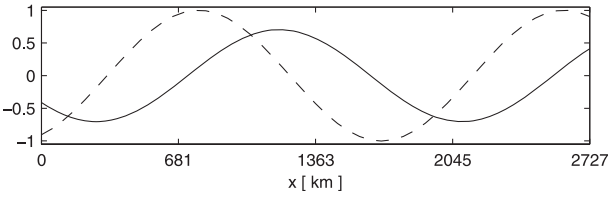

FIG. 6. Convective (solid) and environmental (dashed) downdrafts in the most unstable moist gravity wave for $\Delta_m\theta_e = 11$ K. Curves are normalized by the amplitude of the environmental downdrafts.

Convective and environmental downdraft velocities are plotted in Fig. 6. Their amplitudes are of the same order of magnitude—the environmental downdrafts are slightly larger—but their phases are different, with the environmental contribution lagging the convective by a quarter wavelength. The convective downdraft peaks in the region of strong stratiform heating, in agreement with (14). The environmental downdraft, however, peaks in the suppressed phase of the wave, which is characterized by tropospheric cooling and low-level descent. The overall effect of the environmental downdrafts is therefore to increase the amplitude and phase lag of the downdraft velocity M_d'.

The boundary layer velocity budget (Fig. 7a) is dominated by the pressure gradient term. The free troposphere contributions from θ_1' and θ_2' are an order of magnitude larger than the internal boundary layer fluctuations from θ_b' (Fig. 7b). The boundary layer velocity and consequently environmental downdrafts are therefore driven mainly by mechanical coupling with the free troposphere. The effect of this coupling is to accelerate the boundary layer during the convective phase of the wave, which forces environmental downdrafts in the suppressed phase. Momentum entrainment is small compared to the pressure gradient, and in any case is substantially offset by surface drag.

The θ_{eb}' budget (Fig. 8a) has downdraft, entrainment, and surface flux contributions of comparable amplitudes. Downdrafts and entrainment are approximately in phase and moisten the boundary layer in advance of deep convection. The negative downdraft and entrainment perturbations in this phase of the wave counteract the background subsidence of dry midtropospheric air, which forces a positive θ_{eb}' anomaly. After deep convection in the stratiform and suppressed phase of the wave, when the ABL is relatively dry, θ_{eb}' is further reduced by positive downdraft and entrainment perturbations. The tendency of downdrafts to reinforce θ_{eb}' perturbations is significantly enhanced by the inclusion of environmental downdrafts and entrainment, which explains the substantial increase in growth rate when ABL dynamics are included.

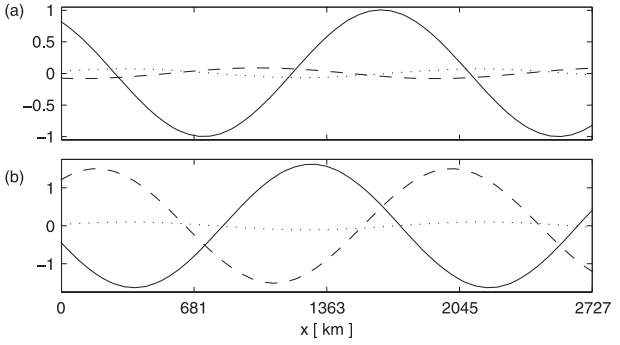

FIG. 7. (a) Budget of u_b' in the most unstable moist gravity wave for $\Delta_m\theta_e = 11$ K, separated into contributions from the pressure gradient (solid), entrainment (dashed), and surface drag (dotted). (b) Contributions to pressure gradient force from θ_1' (solid), θ_2' (dashed), and θ_b' (dotted). Curves are normalized by the amplitude of the total pressure gradient.

The budget of boundary layer potential temperature is different from that of θ_{eb}' (Fig. 8b). Downdrafts warm the boundary layer following deep convection and into the suppressed phase of the wave, whereas entrainment and surface fluxes cool it. Although the midtroposphere—where downdrafts originate—is cooled by stratiform precipitation when convective downdrafts are active, the total effect of downdrafts is nevertheless to increase θ_b' (see Stevens 2005). However, this warming is more than offset by the drying effects of downdrafts, so the overall tendency of θ_{eb}' is not significantly affected.

For larger values of $\Delta_m\overline{\theta}_e$, the wavenumber and phase speed of the most unstable moist gravity wave are diminished, from $k = 22$ and $c_p = 15$ m s^{-1} for $\Delta_m\overline{\theta}_e = 11$ to $k = 14$ and $c_p = 5.5$ m s^{-1} for $\Delta_m\overline{\theta}_e = 15$ K (Table 5). The basic wave structure seen in Fig. 5 persists into this regime, although the relative magnitude of environmental downdrafts is enhanced. For a sufficiently dry basic state—specifically, as $\Delta_m\overline{\theta}_e$ goes from

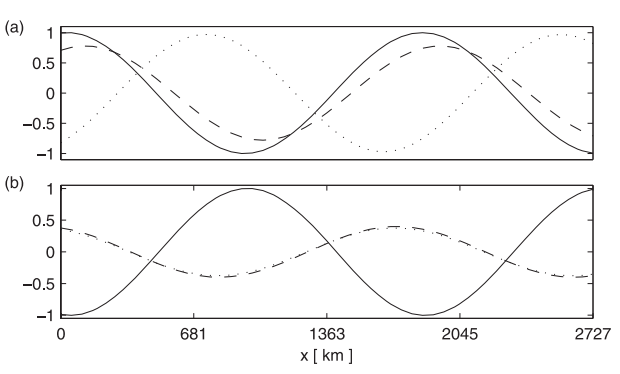

FIG. 8. Budget of (a) θ_{eb}' and (b) θ_b' in the most unstable moist gravity wave for $\Delta_m\theta_e = 11$ K, separated into contributions from downdrafts (solid), entrainment (dashed), and surface fluxes (dotted). Curves are normalized by the downdraft contribution.

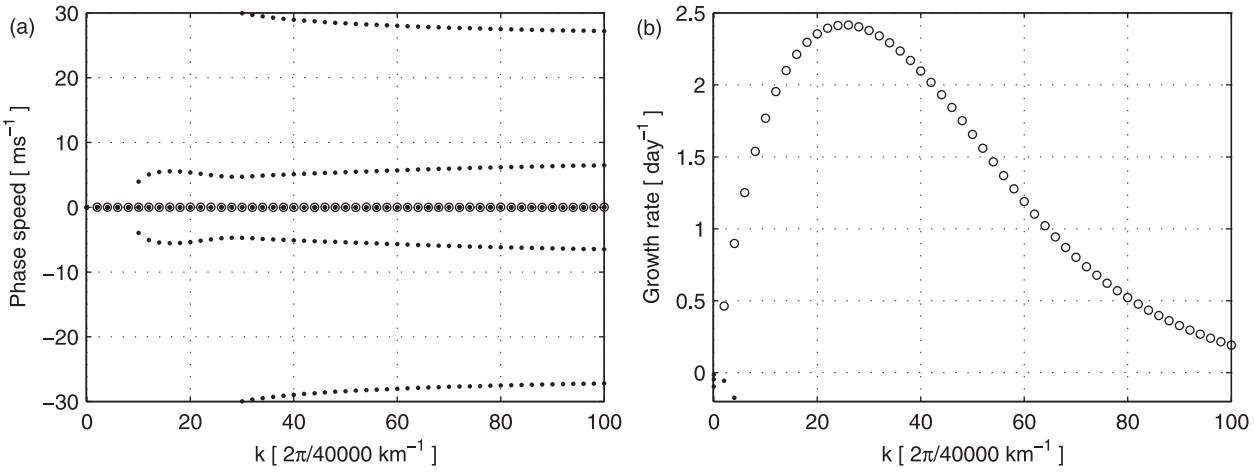

FIG. 9. (a) Phase speeds and (b) growth rates as a function of wavenumber for a dry RCE with $\Delta_m\theta_e = 17$ K. Unstable modes are drawn as open circles and stable modes as dots.

15 to 16 K—the moist gravity wave instability disappears. As described by K&M, it is replaced by congestus standing wave instability, which is discussed next.

b. Synoptic-scale congestus instability

The phase speeds and growth rates for $\Delta_m\overline{\theta}_e = 17$ K are plotted in Fig. 9. A congestus standing wave instability is present over a wide range of wavenumbers, from planetary modes with $k = 1$ to mesoscale modes with $k > 100$. The growth rate peaks at 2.4 day^{-1} for $k = 25$, which corresponds to a synoptic-scale wavelength of 1600 km. The existence of a large-scale maximum growth rate is in contrast to the results of K&M, who found the growth rate to monotonically approach a relatively small value at large k. Boundary layer dynamics therefore introduce a preferred scale for the congestus standing wave. The wave stabilizes for $k \gtrsim 100$, although for even drier regimes the growth rate approaches a small nonnegative value at large k (Table 5).

The structure of the most unstable standing wave is shown in Fig. 10. Heating is dominated by congestus and deep convection and consequently peaks in the lower troposphere (Fig. 10a), where temperature perturbations are the strongest (Fig. 10b). Heating, temperature, and vertical velocity are in exactly in phase; there is no vertical tilt, consistent with the standing nature of the wave. The flow is thermally direct, with tropospheric updrafts in the warm anomalies and downdrafts in the cold anomalies. As was the case for the moist gravity wave, the circulation in the boundary layer follows the lower troposphere (Fig. 10c). Free troposphere and boundary layer moisture are in phase with one another and with convective heating (Fig. 10d). The boundary layer potential temperature, however, has the opposite phase. Warm anomalies in the boundary layer are located directly under cold anomalies in the lower troposphere, where environmental downdrafts are maximum. Interestingly, the stratiform standing wave (Table 5) has a similar structure, but with heating dominated by stratiform and deep convection (not shown).

The downdrafts in the congestus standing wave are almost entirely environmental (Fig. 11). The dominant role of environmental downdrafts explains why the congestus mode exhibits larger growth rates than is the case without an active boundary layer. Convective

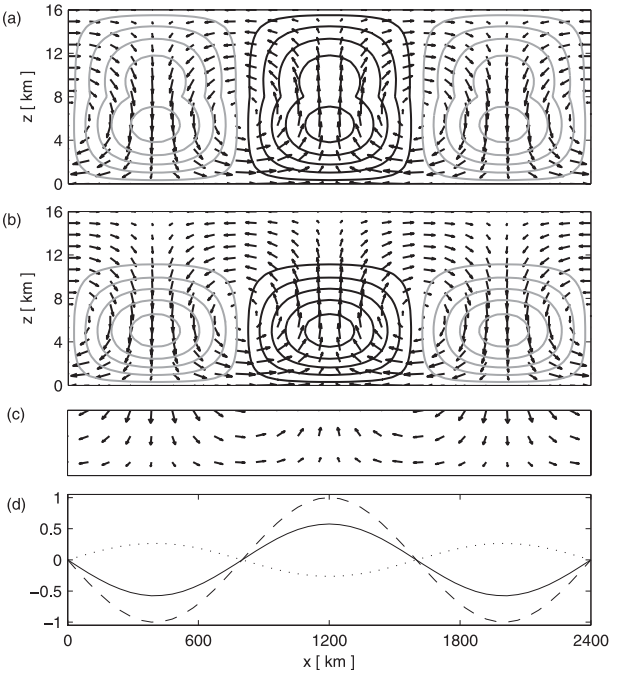

FIG. 10. As in Fig. 5, but for the most unstable congestus standing wave for $\Delta_m\theta_e = 17$ K.

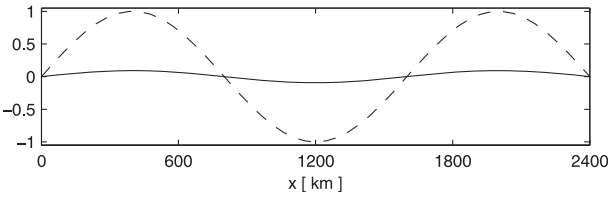

FIG. 11. As in Fig. 6, but for the most unstable congestus standing wave for $\Delta_m\theta_e = 17$ K.

downdrafts have the same phase as environmental ones but are an order of magnitude weaker. The ABL pressure gradient has a stronger internal contribution from θ_b' than in the moist gravity wave but is nevertheless dominated by free troposphere pressure (not shown). This gradient, along with the entrainment of lower tropospheric momentum, acts to reinforce the boundary layer velocity perturbations (Figs. 10a,b) and to drive the environmental downdrafts. These downdrafts in turn dominate the thermodynamic evolution of the ABL by warming and drying it in the descending phase of the wave, thereby amplifying the perturbations of θ_b' and θ_{eb}' (Fig. 10d). For θ_b', the warming effects of downdrafts are reduced somewhat by entrainment, which mixes anomalously cool lower-tropospheric air into the warm regions of the boundary layer. By contrast, the drying effects of downdrafts are enhanced by entrainment of anomalously dry air into the boundary layer.

c. Role of environmental downdrafts

Environmental downdrafts play a prominent role in both the moist gravity wave and standing wave instabilities described above. Indeed, with an active boundary layer it is essential to include the environmental contribution $h_b\nabla \cdot \mathbf{u}_b$ in the definition (15) of M_d. Without it, transport across $z = 0$ by w_0 is identified with entrainment because the $h_b\nabla \cdot \mathbf{u}_b$ in (3) is not cancelled by the environmental contribution in M_d. This assignment of boundary layer divergence to entrainment is unphysical because the induced vertical velocity w_0 extends well into the free troposphere and is not restricted to low levels where boundary layer entrainment is active (Fig. 1). In fact, omitting the environmental contribution in M_d leads to a spurious short-wave instability in both moist and dry regimes (not shown). For $\Delta_m\overline{\theta}_e = 11$ K, this instability emerges for $k \gtrsim 150$ and involves a nonpropagating disturbance; for $\Delta_m\overline{\theta}_e = 17$ K, it is confined to smaller scales with $k \gtrsim 600$ and has a small nonzero phase speed of around 1 m s^{-1}. In both cases, the growth rate increases linearly with wavenumber, yielding a catastrophic blowup of the smallest scales in the model when sufficiently high horizontal resolution is employed.

On the other hand, having included environmental downdrafts in our definition of M_d, can we then neglect the convective contribution? In the absence of environmental downdrafts, eliminating convective downdrafts by setting $\mu = 0$ has a stabilizing effect on the moist gravity wave. The maximum growth rate decreases by a substantial amount that depends on $\Delta_m\overline{\theta}_e$: for moist regimes with $\Delta_m\overline{\theta}_e = 11$ K, the reduction in growth rate is around 25%, whereas for an intermediate regime with $\Delta_m\overline{\theta}_e = 14$ K, the wave is essentially stabilized. With a dynamically active boundary layer, however, environmental downdrafts act even when convective downdrafts are eliminated. Setting $\mu = 0$ in the present model leads to a negligible increase in growth rate and a slight decrease in phase speed of the unstable moist gravity wave (see Table 7, where the sensitivity to various parameters, including μ, is summarized). Without a convective contribution, the total perturbation downdraft velocity is shifted to the left, as expected from Fig. 6. The associated drying of the boundary layer becomes more in phase with the negative anomalies of θ_{eb}', which amplifies the growth and slows the propagation of the wave. For the standing wave instability, eliminating convective downdrafts reduces the growth rate by around 10%, which is consistent with the weak convective contribution to M_d' seen in Fig. 11.

d. Sensitivity to boundary layer and convective parameters

The model developed here employs nine parameters that were not present in the work of K&M: α_m, κ, γ, Q_{Rb}, τ_T, $\tilde{Q}_0$, $\Delta_s\overline{\theta}$, $\Delta_t\overline{\theta}$, and $\Delta_t\overline{\theta}_e$. Of these, Q_{Rb} is determined at RCE (see section 2e) and $\tilde{Q}_0$ is a function of other parameters (see section 2b). The sensitivity of the moist gravity wave instability to the values of the remaining parameters is summarized in Table 7.

The jumps in θ and θ_e across the ABL top at RCE have a minor effect on wave instability. In particular, letting $\Delta_t\overline{\theta}$ be nonzero decreases the maximum growth rate, but the phase speed is essentially unchanged. The dependence on $\Delta_s\overline{\theta}$ is similarly small. Increasing γ and α_m leads to smaller growth rates and larger phase speeds; increasing κ leads to enhanced growth rates and reduced phase speeds; and increasing τ_T leads to larger growth rates and phase speeds. The overall sensitivity, however, is very weak. Indeed, for all values considered, the most unstable moist gravity wave for $\Delta_m\overline{\theta}_e = 11$ K has a wavenumber between 17 and 28, phase speed between 12 and 16 m s^{-1}, and growth rate between 0.44 and 1.5 day^{-1}. The growth rate of the congestus mode has a similar dependence on these parameters.

The structure of the unstable moist gravity wave is fairly robust to the boundary layer parameters, with the

TABLE 7. Sensitivity of moist gravity wave instability for $\Delta_m\overline{\theta}_e = 11$ K to boundary layer parameters. Apart from the stated values, all parameters are as in Tables 1, 2, and 4.

Parameter	Instability wavenumber band	Wavenumber of most unstable wave	Growth rate (day^{-1}) of most unstable wave	Phase speed ($m\ s^{-1}$) of most unstable wave
Standard	$1 \le k \le 47$	22	0.79	15.0
$\Delta_s\overline{\theta} = 1$ K	$1 \le k \le 45$	21	0.75	15.1
$\Delta_s\overline{\theta} = 3$ K	$1 \le k \le 40$	19	0.64	15.2
$\Delta_s\overline{\theta} = -2$ K	$1 \le k \le 41$	20	0.69	15.1
$\Delta_s\overline{\theta} = -5$ K	$1 \le k \le 34$	17	0.56	15.2
$\Delta_s\overline{\theta}_e = 1$ K	$1 \le k \le 42$	20	0.84	14.7
$\Delta_s\overline{\theta}_e = 8$ K	$1 \le k \le 50$	23	0.80	15.2
$\gamma = 0.2$	$1 \le k \le 49$	22	0.85	14.9
$\gamma = 0.75$	$1 \le k \le 45$	21	0.75	15.1
$\gamma = 1$	$1 \le k \le 43$	20	0.71	15.2
$\alpha_m = 0.1$	$1 \le k \le 49$	22	0.87	14.9
$\alpha_m = 0.5$	$1 \le k \le 42$	20	0.62	15.5
$\alpha_m = 1$	$1 \le k \le 37$	20	0.44	16.1
$\kappa = 3$	$1 \le k \le 55$	24	1.0	14.6
$\kappa = 5$	$1 \le k \le 72$	28	1.5	14.0
$\tau_T = 4$ h	$1 \le k \le 45$	21	0.79	15.0
$\tau_T = 16$ h	$1 \le k \le 48$	22	0.81	15.1
$\mu = 0$	$1 \le k \le 55$	22	0.81	12.8

exception of α_m. This parameter has a significant effect on the relative size of the environmental and convective contributions to M_d'. Downdrafts are mostly environmental for small α_m and primarily convective for large α_m; the phase lag between the environmental and convective contributions, however, is unaffected. The critical value of α_m at which environmental and convective downdrafts have equal amplitudes is approximately 0.3, which is close to the standard value employed here.

The dependence of the synoptic-scale moist gravity wave on convective parameters is consistent with the findings of K&M. In particular, we consider sensitivity to the deep convective parameters a_0, a_1, and τ_{conv}, where a_0 characterizes the contribution of θ_1 and θ_2 to H_d, a_1 measures the contribution of θ_{eb} to H_d, and τ_{conv} is the convective time scale. The maximum growth rate decreases for increasing a_0 and τ_{conv} and decreasing a_1. Significantly, the mesoscale fast gravity wave instability is present for a wide range of convective parameter values. Indeed, it appears whenever the synoptic scale-wave is unstable and is therefore not a spurious result due to a fortuitous combination of parameters. As a_0 increases, the growth rate of the fast gravity wave decreases, with the result that the instability is restricted to even larger wavenumbers, where the physical validity of the model is questionable.

4. Conclusions

We have presented an intermediate model for convectively coupled waves that explicitly incorporates boundary layer dynamics and environmental downdrafts in a multicloud framework for congestus, deep, and stratiform convection. The model couples bulk ABL equations for velocity, potential temperature, and moist entropy, derived following S06, with the free troposphere multicloud equations of K&M. A barotropic velocity mode is included, and its nonzero horizontal divergence is slaved to the boundary layer flow to ensure continuity of vertical velocity (as in Biello and Majda 2004; Sobel and Neelin 2006). Flow through the top of the ABL, which we identify with environmental downdrafts, supplements the evaporation-driven convective downdrafts and enhances the flux of dry mid-tropospheric air into the boundary layer. The boundary layer pressure, which plays an important role in driving the environmental downdrafts, is found by matching with the pressure at the base of the free troposphere. The assumption of fixed ABL depth is made consistent with mass conservation through the entrainment of lower free troposphere air into the boundary layer.

The overall effect of including boundary layer dynamics in the multicloud model is to enhance the instability of the synoptic-scale moist gravity and congestus waves. For both classes of waves, ABL dynamics increase the maximum growth rate by an order of magnitude without significantly altering the free tropospheric structure and phase speed of the most unstable waves. The moist gravity wave has a phase speed of 10–20 $m\ s^{-1}$ and vertical tilt, with boundary layer convergence leading congestus heating, which leads deep convective heating, which in turn leads stratiform heating. The congestus

wave is nonpropagating and exhibits free troposphere and ABL updrafts in regions of congestus and deep convection. The enhanced instability of these waves is due to the drying of the ABL by environmental downdrafts and entrainment, which is strongest in the dry boundary layer phase of the wave. For the moist gravity wave, the growth rate peaks at synoptic scales, yielding a dominant wavelength of a few thousand kilometers as found by K&M. For the congestus instability, boundary layer dynamics and environmental downdrafts introduce a preferred synoptic scale, which does not occur with a purely thermodynamic ABL.

In addition to the familiar moist gravity and congestus waves, ABL dynamics destabilize a mesoscale gravity wave, which exhibits a second baroclinic structure coupled with deep convection. The phase speed is 26 m s^{-1}, which is slightly faster than that of the dry second baroclinic gravity wave. This instability is present for all but the driest tropospheric regimes. Its growth rate, though nonnegligible, is consistently smaller than that of the dominant synoptic-scale mode (moist gravity wave or congestus wave, depending on the basic state). The origin and relevance of this instability requires further investigation. It may be related to the second baroclinic waves that are excited by localized deep convection (e.g., Stechmann et al. 2008) or to the myriad of high-frequency inertia–gravity waves that are excited by diurnal variations of deep convection, as reported by G. Kiladis and others (2008, personal communication). It is robust to changes in boundary layer and convective parameters; its sensitivity to the ABL entrainment, however, remains to be established.

The coupled ABL/multicloud model presented here provides a natural framework for the study of convectively coupled waves in a variety of regimes. The explicit representation of potential temperature in the ABL allows for a straightforward separation of sensible and latent heat fluxes, making the model suitable for midlatitude regimes and for the study of land–sea contrast and the diurnal cycle. With an improved representation of boundary layer entrainment, the model could be extended to investigate the effects of cloud–radiation feedback on wave stability. Finally, the full two-dimensional dynamics of the barotropic mode in the free troposphere, along with its coupling to the ABL through environmental downdrafts, may destabilize convectively coupled Rossby waves that were missing in KM08b, since they are often observed to evolve in environments with strong barotropic flow (Wheeler et al. 2000).

Acknowledgments. MLW is supported through a Pacific Institute for the Mathematical Sciences postdoctoral fellowship as part of the Collaborative Research Group on Mathematical Problems in Climate Modelling. The research of BK is partly supported by a grant from the Natural Sciences and Engineering Research Council of Canada. Helpful comments and suggestions from Andrew Majda, Bjorn Stevens, and Joseph Biello are gratefully acknowledged.

APPENDIX

Boundary Layer Equations

The boundary layer equations [(1a)–(1c)] are derived following S06. The Reynolds-averaged advection equation for a scalar ϕ (θ or θ_e) is

$$\partial_t\langle\phi\rangle + \langle\mathbf{u}\rangle\cdot\nabla\langle\phi\rangle + \langle w\rangle\partial_z\langle\phi\rangle = -\partial_z\langle w'\phi'\rangle + \langle F\rangle, \tag{A1}$$

where F is a forcing, $\langle\cdot\rangle$ denotes Reynolds average, primes (in this appendix only) denote fluctuation from Reynolds average, and horizontal turbulent fluxes have been neglected. Defining ϕ_b to be the vertical average of $\langle\phi\rangle$ over the ABL, it is straightforward to show that

$$\partial_t\phi_b + \nabla\cdot(\mathbf{u}_b\phi_b) + \frac{1}{h_b}\langle w_t\rangle\langle\phi_t\rangle = -\frac{1}{h_b}\langle w'\phi'\rangle_t + \frac{1}{h_b}\langle w'\phi'\rangle_s + F_b, \tag{A2}$$

where the subscripts s and t denote evaluation at $z = -h_b$ and $z = 0$ approached from above, respectively; we have replaced $(\langle\mathbf{u}\rangle\langle\phi\rangle)_b$ with $\mathbf{u}_b\phi_b$. The equation for $\mathbf{u}_b$ is derived in a similar fashion.

The boundary layer Eqs. (1) follow from (A2) by specifying $\langle w'\phi'\rangle_s$ and $\langle w'\phi'\rangle_t$ as follows: Surface fluxes are defined following K&M as

$$\langle w'\phi'\rangle_s \equiv \frac{h_b}{\tau_e}(\phi_s - \phi_b), \quad \langle w'\mathbf{u}'\rangle_s \equiv -C_d U\,\mathbf{u}_b. \tag{A3}$$

Fluxes through the top of the boundary layer are written following S06 as

$$\langle w'\phi'\rangle_t \equiv M_u(\phi_b - \phi_t) - M_d(\phi_m - \phi_t),$$
$$\langle w'\mathbf{u}'\rangle_t \equiv \frac{h_b}{\tau_T}(\mathbf{u}_b - \mathbf{u}_t). \tag{A4}$$

This formulation admits the important effect of downdrafts on the thermodynamic budget of the ABL without making any assumptions about the nature of convective momentum transport.

REFERENCES

Albrecht, B. A., A. K. Betts, W. H. Shubert, and S. K. Cox, 1979: Model of the thermodynamic structure of the trade-wind boundary layer. Part I: Theoretical formulation and sensitivity tests. *J. Atmos. Sci.,* **36,** 73–89.

Arakawa, A., and W. H. Shubert, 1974: Interaction of a cumulus cloud ensemble with the large-scale environment, Part I. *J. Atmos. Sci.,* **31,** 674–701.

Bellon, G., and B. Stevens, 2005: On bulk models of shallow cumulus convection. *J. Atmos. Sci.,* **62,** 3286–3302.

Betts, A. K., 1976: Modeling subcloud layer structure and interaction with a shallow cumulus layer. *J. Atmos. Sci.,* **33,** 2363–2382.

——, and W. Ridgway, 1989: Climatic equilibrium of the atmospheric convective boundary layer over a tropical ocean. *J. Atmos. Sci.,* **46,** 2621–2641.

Biello, J. A., and A. J. Majda, 2004: Boundary layer dissipation and the nonlinear interaction of equatorial baroclinic and barotropic Rossby waves. *Geophys. Astrophys. Fluid Dyn.,* **98,** 85–127.

Emanuel, K. A., 1994: *Atmospheric Convection*. Oxford University Press, 580 pp

——, J. D. Neelin, and C. S. Bretherton, 1994: On large-scale circulation in convecting atmospheres. *Quart. J. Roy. Meteor. Soc.,* **120,** 1111–1143.

Firestone, J. K., and B. A. Albrecht, 1986: The structure of the atmospheric boundary layer in the central equatorial Pacific during January and February of FGGE. *Mon. Wea. Rev.,* **114,** 2219–2231.

Johnson, R. H., T. M. Rickenbach, S. A. Rutledge, P. E. Ciesielski, and W. H. Schubert, 1999: Trimodal characteristics of tropical convection. *J. Climate,* **12,** 2397–2418.

——, P. E. Ciesielski, and J. A. Cotturone, 2001: Multiscale variability of the atmospheric mixed layer over the western Pacific warm pool. *J. Atmos. Sci.,* **58,** 2729–2750.

Khouider, B., and A. J. Majda, 2006a: A simple multicloud parameterization for convectively coupled tropical waves. Part I: Linear analysis. *J. Atmos. Sci.,* **63,** 1308–1323.

——, and ——, 2006b: Multicloud convective parameterizations with crude vertical resolution. *Theor. Comput. Fluid Dyn.,* **20,** 351–375.

——, and ——, 2007: A simple multicloud parameterization for convectively coupled tropical waves. Part II: Nonlinear simulations. *J. Atmos. Sci.,* **64,** 381–400.

——, and ——, 2008a: Multicloud models for organized tropical convection: Enhanced congestus heating. *J. Atmos. Sci.,* **65,** 895–914.

——, and ——, 2008b: Equatorial convectively coupled waves in a simple multicloud model. *J. Atmos. Sci.,* **65,** 3376–3397.

——, ——, and M. Katsoulakis, 2003: Coarse-grained stochastic models for tropical convection. *Proc. Natl. Acad. Sci. USA,* **100,** 11 941–11 946.

Kiladis, G. N., K. H. Straub, and P. K. Haertl, 2005: Zonal and vertical structure of the Madden–Julian oscillation. *J. Atmos. Sci.,* **62,** 2790–2809.

Kraus, E. B., and H. P. Hanson, 1974: Climatological aspects of the tropical convective boundary layer. *Bound.-Layer Meteor.,* **6,** 219–233.

Larsen, K., D. L. Hartmann, and S. A. Klein, 1999: The role of clouds, water vapor, circulation, and boundary layer structure in the sensitivity of the tropical climate. *J. Climate,* **12,** 2359–2374.

Lin, X., and R. H. Johnson, 1996: Kinematic and thermodynamic characteristics of the flow over the western Pacific warm pool during TOGA COARE. *J. Atmos. Sci.,* **53,** 695–715.

Majda, A. J., 2003: *Introduction to PDEs and Waves for the Atmosphere and Ocean*. American Mathematical Society, 234 pp.

——, and M. Shefter, 2001a: Waves and instabilities for model tropical convective parameterizations. *J. Atmos. Sci.,* **58,** 896–914.

——, and ——, 2001b: Models for stratiform instability and convectively coupled waves. *J. Atmos. Sci.,* **58,** 1567–1584.

——, and B. Khouider, 2002: Stochastic and mesoscopic models for tropical convection. *Proc. Natl. Acad. Sci. USA,* **99,** 1123–1128.

Mapes, B. E., 2000: Convective inhibition, subgrid-scale triggering energy, and stratiform instability in a toy tropical wave model. *J. Atmos. Sci.,* **57,** 1515–1535.

Neggers, R., B. Stevens, and J. D. Neelin, 2006: A simple equilibrium model for shallow cumulus topped mixed layers. *Theor. Comput. Fluid Dyn.,* **20,** 305–322.

Raymond, D. J., 1995: Regulation of moist convection over the west Pacific warm pool. *J. Atmos. Sci.,* **52,** 3945–3959.

Sobel, A. H., and J. D. Neelin, 2006: The boundary layer contribution to intertropical convergence zones in the quasi-equilibrium tropical circulation model framework. *Theor. Comput. Fluid Dyn.,* **20,** 323–350.

Stechmann, S. N., A. J. Majda, and B. Khouider, 2008: Nonlinear dynamics of hydrostatic internal gravity waves. *Theor. Comput. Fluid Dyn.,* **22,** 407–432, doi:10.1007/S00162-008-0080-7.

Stevens, B., 2005: Atmospheric moist convection. *Annu. Rev. Earth Planet. Sci.,* **33,** 605–643.

——, 2006: Bulk boundary-layer concepts for simplified models of tropical dynamics. *Theor. Comput. Fluid Dyn.,* **20,** 279–304.

Straub, K. H., and G. N. Kiladis, 2003: The observed structure of convectively coupled Kelvin waves: Comparisons with simple models of coupled wave instability. *J. Atmos. Sci.,* **60,** 1655–1668.

Stull, R. B., 1988: *An Introduction to Boundary Layer Meteorology*. Kluwer, 666 pp.

Tulich, S. N., D. A. Randall, and B. E. Mapes, 2007: Vertical-mode and cloud decomposition of large-scale convectively coupled gravity waves in a two-dimensional cloud-resolving model. *J. Atmos. Sci.,* **64,** 1210–1229.

Wheeler, M., and G. N. Kiladis, 1999: Convectively coupled equatorial waves: Analysis of clouds and temperature in the wavenumber–frequency domain. *J. Atmos. Sci.,* **56,** 374–399.

——, ——, and P. J. Webster, 2000: Large-scale dynamical fields associated with convectively coupled equatorial waves. *J. Atmos. Sci.,* **57,** 613–640.

Yano, J.-I., J. C. McWilliams, M. Moncrieff, and K. A. Emanuel, 1995: Hierarchical tropical cloud systems in an analog shallow-water model. *J. Atmos. Sci.,* **52,** 1723–1742.

——, M. W. Moncrieff, and J. C. McWilliams, 1998: Linear stability and single column analyses of several cumulus parametrization categories in a shallow-water model. *Quart. J. Roy. Meteor. Soc.,* **124,** 983–1005.